Supplementary Materials

Monsoons, plumes, and blooms: intraseasonal variability of subsurface primary productivity in the Bay of Bengal

Tamara L Schlosser[1], Andrew J Lucas[1,2], Melissa Omand[3], and J. Thomas Farrar[4]

[1]Scripps Institution of Oceanography, University of California, San Diego, La Jolla, CA, USA.
[2]Dept. of Mechanical and Aerospace Engineering, University of California, San Diego, La Jolla, CA, USA.
[3]Graduate School of Oceanography, University of Rhode Island, Narragansett, RI 02882, USA.
[4]Department of Physical Oceanography, Woods Hole Oceanographic Institution, Woods Hole, MA 02543, USA.

Correspondence: Tamara L Schlosser (tamara.schlosser@utas.edu.au)

S1 Additional Data Analysis

S1.1 Subsurface irradiance, attenuation, and PAR

The vertical change in irradiance, I ($\mu\mathrm{W\,cm^{-2}\,nm^{-1}}$), was spectrally decomposed into numerous wavelengths via:

$$I(\lambda,z,t) = I_0(t)\sum a(\lambda)e^{-K_d(\lambda,t)z}, \tag{1}$$

where λ is the individual wavelength, K_d is the diffuse attenuation coefficient over depth z, I_0 is the subsurface irradiance magnitude near the surface, and a is the irradiance magnitude at each λ. We collected irradiance measurements at four wavelengths $380\,\mathrm{nm}$, $412\,\mathrm{nm}$, $490\,\mathrm{nm}$ and $532\,\mathrm{nm}$ using a Satlantic OCR-504. The observed irradiance decreased around noon over the upper $15\,\mathrm{m}$ due to shading by the buoy. To correct this buoy shading, we assume shortwave radiation, I_0^+, and the surface irradiance at each wavelength, $I_0(\lambda,t)$, are linearly correlated such that:

$$I_0^+(t) \approx I_0(\lambda,t) \times a(\lambda,t), \tag{2}$$

where we derive the constant a as the median $I_0^+/I_0(\lambda,t)$ during daylight on each day sampled (further details below). We additionally tested fitting irradiance over the full water-column (i.e., depth-constant $K_d[t]$) and fitting over $2.5\,\mathrm{m}$ depth ranges (i.e., depth-variable $K_d[z,t]$). Although the depth-variable diffuse attenuation varied somewhat in the vertical, particularly where ChlF and turbidity were enhanced, the variability was relatively weak and did not change the main results, and hence we used the simpler depth-constant approach (Figure S1).

The raw irradiance measurements required some quality control and correction. At M2, $I(380,t)$ and $I(412,t)$ degraded at approximately $I < 1.9\,\mathrm{\mu W\,cm^{-2}\,nm^{-1}}$. We hence removed all measurements below this threshold and for these wavelengths at M2. We removed all measurements when $I(\lambda,t)$ increased with depth, vertically smooth over $4\,\mathrm{m}$ and then bin in time into $3\,\mathrm{h}$ bins. We also bin I_0^+ into $3\,\mathrm{h}$ bins.

We next least-squares fit $I(\lambda,t)$ to an exponential curve and find both $K_d(\lambda,t)$ and $I_0(\lambda,t) \times a(\lambda,t)$ such that the mean absolute error (MAE) is minimized, where we find the MAE using:

$$\mathrm{MAE}(\lambda) = \frac{1}{n} \sum \|I(\lambda,t) - I_{fit}(\lambda,t)\|, \tag{3}$$

where n is the number of samples and $I_{fit}(\lambda,t)$ is the least-squares fitted irradiance at the same wavelength. We exclude fits if MAE$\geq 5\,\mu\mathrm{W\,cm^{-2}\,nm^{-1}}$. We then compared the estimated $I_0(\lambda,t)$ to I_0^+ and find an excellent agreement with a correlation coefficient (r^2) exceeding 0.9 at all profilers, where at M3 we used the M2 I_0^+ measurement.

Lastly, we interpolated the 3-h binned $K_d(\lambda,t)$ to the observed $\mathcal{O}(10\,\mathrm{min})$ time-step. Instead of interpolating the binned $I_0(\lambda,t)$, we make use of the high fidelity observations of shortwave radiation by binning the $1\,\mathrm{min}$ time-step I_0^+ to the profiler time-step, find the median ratio of I_0^+ and $I_0(\lambda,t) \times a(\lambda,t)$ on each day, with both variables binned over $3\,\mathrm{h}$, then multiply the $\mathcal{O}(10\,\mathrm{min})$ time-stepped I_0^+ by this ratio to define a new $I_0(\lambda,t) \times a(\lambda,t)$ with a $\mathcal{O}(10\,\mathrm{min})$ time-step. We then finally recalculate $I(\lambda,z,t)$ using variables with a $\mathcal{O}(10\,\mathrm{min})$ time-step using Equation 1.

The photosynthetically available radiation (PAR) range is from $400\,\mathrm{nm}$ to $700\,\mathrm{nm}$; however, we only observed the wavelengths $380\,\mathrm{nm}$, $412\,\mathrm{nm}$, $490\,\mathrm{nm}$ and $532\,\mathrm{nm}$. We estimate PAR ($\mu\mathrm{mol\,m^{-2}\,s^{-1}}$) by assuming the observed waveranges were representative of the full PAR range via:

$$\mathrm{PAR}(z,t) = \int_{380}^{532} I(\lambda,z,t) d\lambda \times \frac{700-400}{532-380} \times 0.046, \tag{4}$$

where the constant 0.046 was required for the unit conversion.

S1.2 Turbidity and Chlorophyll Fluorescence

We detail the NPQ correction method in the Methods, which employs the co-located irradiance measurements. Corrected ChlF exponentially decays with depth, like irradiance, with small ($<0.05\,\mu\mathrm{g\,L^{-1}}$) magnitudes near the SCM (Figure S2).

Like at profiler M3, at M1 and M2 we observed a prominent SCM with diel cycles in ChlF (Figure S3). At noted in the manuscript, we applied the diel fitting method at these profilers and returned a significant relationship for all but two days during the cloudy active monsoon period at M2 (July 23 and 25). We also note vertical heaving by internal waves was strongest at M1, and although our use of the SCM PAR to model growth accounted for reductions in PAR from this vertical heaving, the performance of the diel cycle fit slightly reduced when heaving was strongest (e.g., July 16).

In addition to ChlF, turbidity can also be a useful proxy for phytoplankton biomass. Within the coastal plume, although both turbidity and ChlF were enhanced above $40\,\mathrm{m}$, below the $1023\,\mathrm{kg\,m^{-3}}$ isopycnal, only turbidity was enhanced (Figure 1d-e). This suggests turbidity was predominantly enhanced due to non-algal sources, such as suspended sediments, rather than biological variability. Outside the plume, at times SCM ChlF and turbidity co-varied but due to the mixed sources of turbidity we use the NPQ-corrected ChlF fluctuations for our following biological analysis.

At M3, we observed a diel cycle in the turbidity at the SCM when ChlF was enhanced and the profiler was not influenced by the coastal plume (Figure S4). The confidence intervals for the rate of gross primary production of turbidity (GPP_τ) were

relatively large compared to $\mathrm{GPP}_{\mathrm{ChlF}}$ (Figure 2d) but estimates of GPP_{τ} more likely represent the change in phytoplankton biomass. The rate of gross primary production of turbidity (GPP_{τ}) was exceeded by the loss rate of turbidity from July 22 to 26, which we also observed in the ChlF signal from July 20 onwards. However, $\mathrm{GPP}_{\mathrm{ChlF}}$ steadily decreased from July 21 while GPP_{τ} sharply decreased on July 22 and remained small. The presence of a diel cycle in both ChlF and turbidity strongly suggests that ChlF represented changes in biomass.

S1.3 BCG-Argo Analysis

We utilized all available BGC-Argo floats in the BoB deployed from 2013 to 2018 with at least a full annual cycle. For each profile, we computed the depth of the SCM where subsurface ChlF was maximum, which had the deepest extent of $140\,\mathrm{m}$. We then computed the depth-averaged ChlF over only the upper $140\,\mathrm{m}$ to describe the subsurface ChlF. As the SCM was isopycnal following, we estimated the SCM ChlF as the depth-averaged ChlF over the $20\,\mathrm{m}$ centred on the $1022\,\mathrm{kg\,m^{-3}}$ isopycnal. For each profile, we matched the profile location to the nearest surface PAR (NASA Goddard Space Flight Center, 2018b) and diffuse attenuation (Goddard Space Flight Center, 2018a) measurement from MODIS, where some spatial smoothing of the MODIS product was required prior to matching the location.

In the Results, we correlated surface PAR to the SCM ChlF for the months of June to October for a single BGC-Argo profiler deployed in 2016 (Figure 4). We also considered the correlation of SCM PAR and ChlF for the other profilers, with profiler observations lasting over 12-months segmented into 12-month chunks (Figure S5). Note the number of samples used (n) varied from 45 to 198, with a median of 72. Of the 26 segments, eight had moderate correlation ($r^2 > 0.2$), all of which were significant ($p < 0.01$). Our in situ observations with the Wirewalker and meteorological buoy suggest that a fairly rapid productivity response to fluctuations in SCM PAR occur on the order of one day (Figure 3). We theorize that the co-variance of SCM PAR and ChlF may not be evident in the other BGC-Argo observations due to the low temporal resolution of profiles, the aliasing of the diel cycle in ChlF, and the relative uncertainties of estimating SCM PAR from satellite. Due to the small spatial scales of clouds in the BoB, surface irradiance can vary by orders of magnitude over lateral scales of $\mathcal{O}(1\,\mathrm{km})$ in the BoB (Adams et al., 2019), which further emphasizes the need to relate co-located observations of PAR and ChlF rather than satellite products that represent a much larger region. BGC-Argo profilers are beginning to be deployed with irradiance measurements, which we expect will lead to an improved ability to assess light-limited productivity in the subtropical oligotrophic ocean.

References

Adams, K., MacKinnon, J., Lucas, A. J., Nash, J., Shroyer, E., and Farrar, J. T.: Multi-platform observations of small-scale lateral mixed layer variability in the northern Bay of Bengal, Deep Sea Research Part II: Topical Studies in Oceanography, 168, 104 629, https://doi.org/10.1016/j.dsr2.2019.07.017, 2019.

Goddard Space Flight Center, Ocean Ecology Laboratory, O. B. P. G.: Moderate-resolution Imaging Spectroradiometer (MODIS) Aqua Downwelling Diffuse Attenuation Coefficient Data; 2018 Reprocessing, NASA OB.DAAC, Greenbelt, MD, USA, https://doi.org/10.5067/AQUA/MODIS/L3M/KD/2018, accessed on 10/20/2021, 2018a.

NASA Goddard Space Flight Center, Ocean Ecology Laboratory, O. B. P. G.: Moderate-resolution Imaging Spectroradiometer (MODIS) Aqua Photosynthetically Available Radiation Data; 2018 Reprocessing, NASA OB.DAAC, Greenbelt, MD, USA, https://doi.org/10.5067/AQUA/MODIS/L3M/PAR/2018, accessed on 10/20/2021, 2018b.

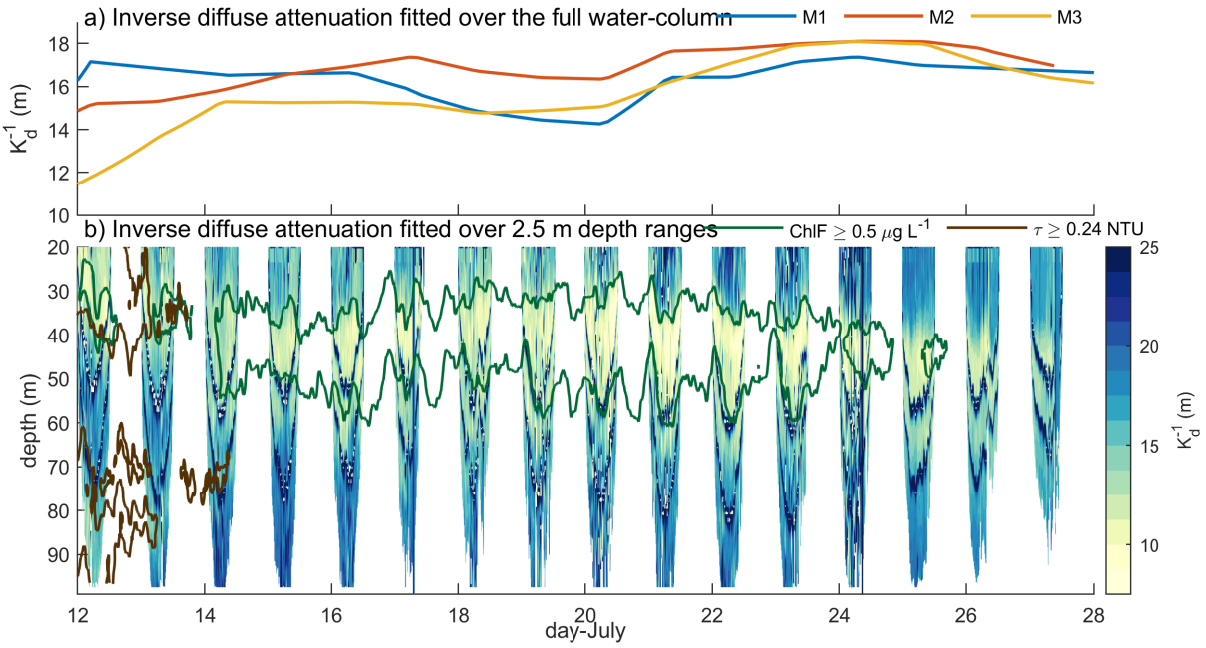

Figure S1. Two estimates of inverse diffuse attenuation. Inverse diffuse attenuation (K_d^{-1}) for a) $K_d(t)^{-1}$ at all profilers and b) $K(z,t)^{-1}$ at M3, with contours indicating high ChlF (green) and turbidity (brown) waters.

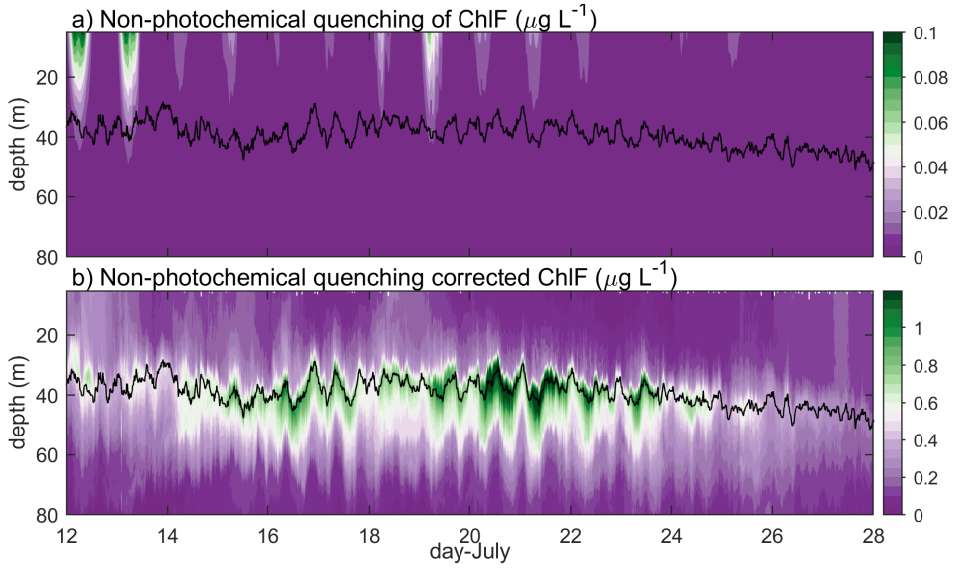

Figure S2. Non-photochemical quenching at M3. a) Estimated non-photochemical quenching (NPQ) correction and b) the corrected ChlF.

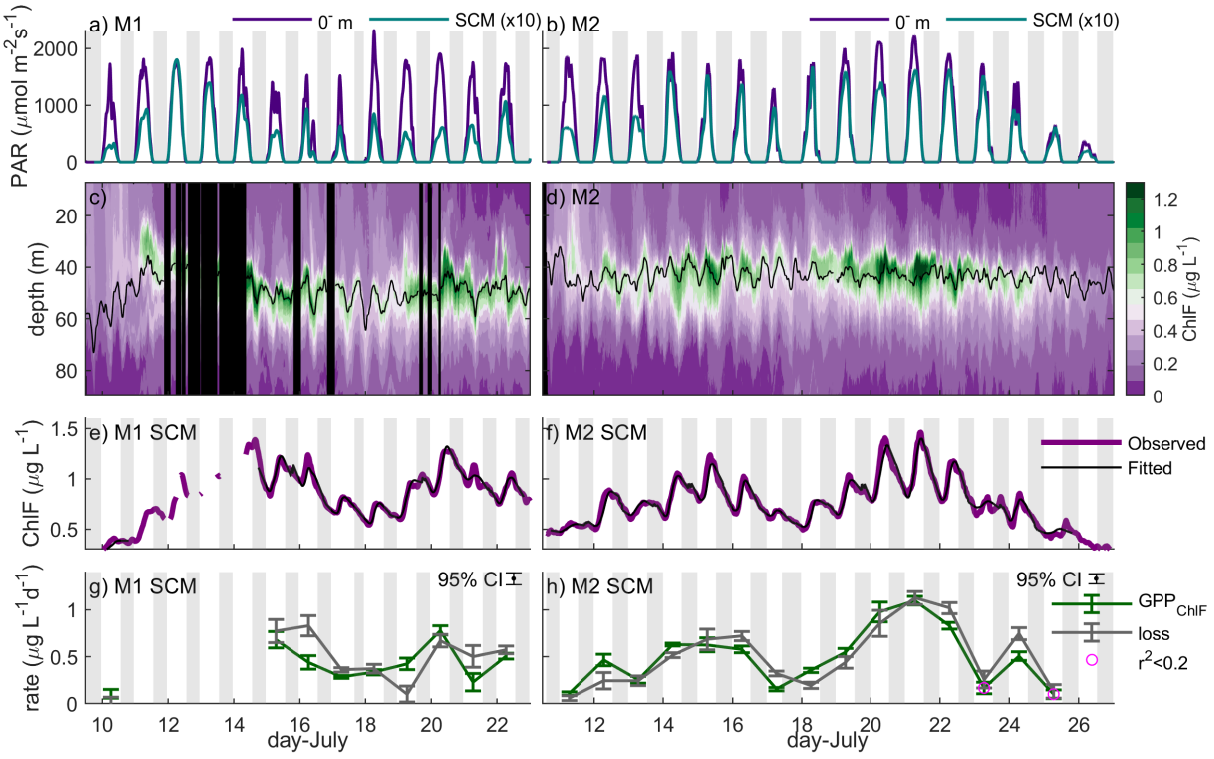

Figure S3. Co-varying light and chlorophyll at M1 and M2. Similar to Figure 2 for M1 (left column) and M2 (right column). The observed ChlF shown in panels c) and d) have no alteration of depth based on isopycnal depth. In h), rates with low correlation coefficient ($r^2 < 0.2$) are indicated.

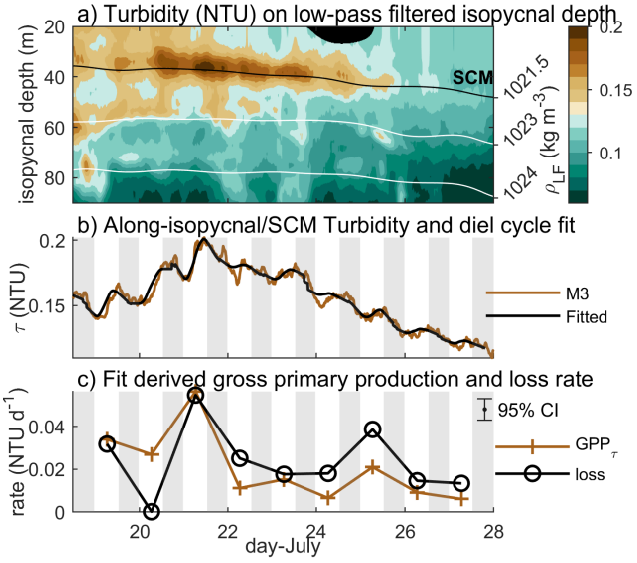

Figure S4. Co-varying light and turbidity. a) Turbidity (τ), with depth representing the 48-h low-pass filtered isopycnal depth (white contour, right y-axis). b) SCM turbidity (τ, brown) and the diel cycle fit (black), and c) the rate of gross τ primary production (GPP_τ, brown) and loss (black).

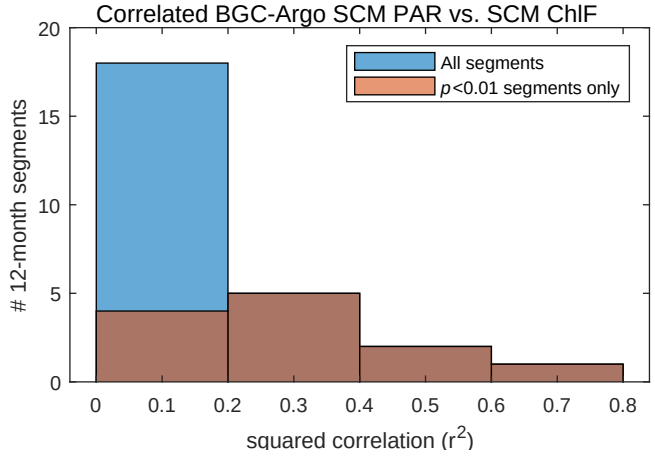

Figure S5. The number of 12-month segmented BGC samples (y-axis) with SCM PAR correlated to SCM ChlF (x-axis), binned by their correlation squared.